Title

A depth-encoding PET detector for high resolution PET using 1 mm SiPMs

Journal

Physics in Medicine and Biology, 65(16)

ISSN

0031-9155

Authors

Du, Junwei
Bai, Xiaowei
Cherry, Simon R

Publication Date

2020-08-21

DOI

10.1088/1361-6560/ab9fc9

Peer reviewed

HHS Public Access

Author manuscript

Phys Med Biol. Author manuscript; available in PMC 2021 December 11.

Published in final edited form as:

Phys Med Biol. ; 65(16): 165011. doi:10.1088/1361-6560/ab9fc9.

A depth-encoding PET detector for high resolution PET using 1 mm SiPMs

Junwei Du, **Xiaowei Bai**, **Simon R Cherry**

Department of Biomedical Engineering, University of California-Davis, One Shields Avenue, Davis, CA 95616, United States of America

Abstract

A dual-ended readout PET detector based on two Hamamatsu 16 × 16 arrays of 1 × 1 mm^2 SiPMs coupled to both ends of a 25 × 25 array of 0.69 × 0.69 × 20 mm^3 polished LYSOs was evaluated in terms of flood histogram, energy resolution, timing resolution, and DOI resolution. The SiPM arrays have a pitch size of 1.2 mm. Each SiPM pixel has an active area of 1 × 1 mm^2, and was fabricated using 15 μm microcells. The LYSO array has a pitch size of 0.75 mm, and the crystals are separated using Toray reflector with a thickness of 50 μm. The flood histogram and energy resolution were measured at different overvoltages (ranging from 1.5 to 7.0 V, in 0.5 V steps) and at four different temperatures (−7, 0, 10 and 20 °C). The timing resolution and DOI resolution were obtained at the optimal overvoltage for the flood histogram and at each different temperature. Overall, the results show better performance was obtained at lower temperatures, and that the optimal overvoltage decreased at higher temperatures. The optimal overvoltage was 5.0 V (corresponding to a bias voltage of 68.5 V) in order to achieve the highest quality flood histogram at 0 °C. Under these conditions, the flood histogram quality, energy resolution, timing resolution, and DOI resolution were 3.26 ± 0.65, 18.4 ± 4.5%, 1.70 ± 0.12 ns and 2.22 ± 0.19 mm, respectively. The flood histograms and energy resolution were also obtained at different activities. The results show that better flood histogram and energy resolution were obtained at lower activity, however all the crystals can be resolved at an event rate of over 210 k cps, indicating the DOI detector module can be used both for high resolution human brain PET and small animal PET applications.

Keywords

PET; DOI; SiPM

1. Introduction

Positron emission tomography (PET) has been broadly applied as a tool in neuroscience research, both in the human brain as well as extensive studies in preclinical models (mouse, rat, nonhuman primate). For human brain studies, PET provides a sensitive and noninvasive window into brain metabolism and neurochemistry, providing information from living human subjects that cannot be obtained using any other techniques. For animal studies,

jwdu@ucdavis.edu .

an advantage of PET is that it allows each animal to be studied repeatedly, hence, each animal can serve as its own control in studies with a longitudinal design. However, currently available PET systems have significant limitations for dynamic imaging studies, and do not simultaneously have performance approaching the theoretical limited of spatial resolution and sufficient detection sensitivity to realize that resolution in most applications (Lehnert et al 2012, Bertoglio et al 2019, Lubberink and Heurling 2019, Nørgaard et al 2019, Zuo et al 2019). The sensitivity is significantly compromised by the use of thinner detectors, limited solid angle coverage, and deadspace/gaps within and between detector modules, and often all three of these effects (Cherry et al 2018).

PET scanners which simultaneously exhibit high sensitivity and high resolution can be constructed using detectors based on photodetectors coupled to both ends of finely segmented, but thick, arrays of scintillation crystals (Shao et al 2014, Yang et al 2016, Du et al 2019). To further improve the sensitivity, the dead space between detector modules can be reduced using detector modules with high packing fraction that minimizes or eliminates gaps between modules (James et al 2010, Gonzalez et al 2018, Du et al 2019). Compared to other depth-encoding methods, excellent and continuous depth-of-interaction (DOI) information can be obtained using the dual-ended readout method (Ito et al 2011).

Silicon photomultipliers (SiPMs) are a perfect choice for building dual-ended DOI-encoding PET detectors, due to their compact size and high gain. Most currently available SiPM-based detectors use SiPM pixels with a pitch size >3 mm to reduce the number of SiPM channels that need to be instrumented (Park and Lee 2019, Pizzichemi et al 2019). This is a good choice for whole-body PET scanners, where spatial resolution is limited to ~2 mm due to the non-colinearity effect, and subject motion tends to be significant, further degrading the actual achievable resolution. However, for high resolution human brain PET scanners and small-animal PET systems, state-of-the-art now dictates the use of crystal arrays with a pitch approaching or even below 1 mm (Gaudin et al 2019, Kochebina et al 2019). While standard (~3 mm) size SiPM arrays can read identify and read out such small crystal elements by using light sharing, the packing fraction is typically very low due to the edge effect encountered in almost all modular detector designs (Yamamoto et al 2013, 2016, Du et al 2019). One solution is using position sensitive SiPMs (PS-SiPMs) (Du et al 2018b), however, this technology is not very mature and is currently limited to a physical size less than 10×10 mm^2. Another solution to improve packing fraction is using SiPM arrays with small pitch size, which is the approach we investigate here.

In this paper, we present a detailed characterization of a DOI detector module based on two Hamamatsu 16×16 SiPM arrays with a pitch size of 1.2 mm coupled to both ends of a 25×25 LYSO scintillator array with a pitch size of 0.75 mm and a length of 20 mm. The packing fraction of the detector module was 95%, similar to previous detector modules designed based on the PS-SiPM arrays (Du et al 2018b).

2. Materials and methods

2.1. DOI detector module

The DOI detector module consisted of two 16 × 16 arrays of S13190 SiPMs and one 25 × 25 array of 0.69 × 0.69 × 20 mm^3 polished LYSO scintillator crystals (figure 1) (Sichuan Tianle Photonics, China). The total surface area of the SiPM array is 19.25 × 19.25 mm^2 and the pitch size is 1.2 mm. Each SiPM pixel has an active area of 1.0 × 1.0 mm^2 in a 1.1 × 1.1 mm^2 package and 4292 microcells with a pitch size of 15 μm. The geometrical fill factor of the SiPMs is 53%, whilst the active area of the SiPM arrays is 69.4 %. The breakdown voltage of the SiPMs is 65.0 V at 25 °C and the temperature coefficient of the breakdown voltage is 60 mV $°C^{-1}$. The LYSO crystal array has a pitch size of 0.75 mm, and Toray reflector with a thickness of 50 μm was used between the crystals. The Toray reflectors were coupled to the LYSO elements using optical glue, and the thickness of the optical glue between crystals is 10 μm. The LYSO array was coupled to the SiPM arrays using optical grease (BC-630, Saint-Gobain, USA) without using any light guide.

2.2. Signal multiplexing circuit

The DOI detector module has a total of 512 SiPM signals. It is impractical to amplify and digitize each SiPM signal individually. To reduce the number of signals for further processing, a signal multiplexing method was designed, as shown in figure 2 (Du et al 2019, Yang et al 2019). In this method, for each of the two SiPM arrays, the anodes of the SiPMs located in the same row were summed to form 16 row signals, and the cathodes in the same column were summed to form 16 column signals. The 16 row signals and 16 column signals were amplified individually and then weighted by applying a gain to each row and column proportional to its location along each axis, generating four position signals (X^+, X^- and Y^+, Y^-) for each SiPM array (Popov et al 2003, Du et al 2016). All the analog operations were implemented using AD8056 amplifiers (Analog Devices, USA). The 8 position signals from the dual-ended detector module were further amplified and shaped using a spectroscopy amplifier (N568B, CAEN, Italy) and digitized using a PowerDAQ board (PD2MFS, United Electronic Industries, USA).

The gamma photon interaction position (x, y), deposited energy (E) and DOI information were calculated as follows using equations (1)–(4):

$$x = \frac{1}{2}\left(\frac{X_1^+ - X_1^-}{X_1^+ + X_1^-} + \frac{X_2^+ - X_2^-}{X_2^+ + X_2^-}\right) \quad (1)$$

$$y = \frac{1}{2}\left(\frac{Y_1^+ - Y_1^-}{Y_1^+ + Y_1^-} + \frac{Y_2^+ - Y_2^-}{Y_2^+ + Y_2^-}\right) \quad (2)$$

$$E = E1 + E2 \quad (3)$$

$$DOI = a\frac{E1 - E2}{E1 + E2} + b \quad (4)$$

where $X_i^+, X_i^-, Y_i^+, Y_i^- (i = 1, 2)$ are the four digitized position signals of the two SiPM arrays, a and b are the calibration parameters for DOI information. $E1 = X_1^+ + X_1^- + Y_1^+ + Y_1^-$ and $E2 = X_2^+ + X_2^- + Y_2^+ + Y_2^-$ were the total energies detected by SiPM 1 and SiPM 2, respectively.

The 32 amplified row signals and 32 amplified column signals of the DOI detector module were summed together to form one timing signal, and sent to constant fraction discriminator (CFD) (Model 584, ORTEC, USA) to generate a time stamp and a trigger for the DAQ board.

2.3. Experimental methods

A 50 μCi ^{22}Na point source with a diameter of 0.25 mm was used in all experiments except in the study of the detector's performance as a function of activity, where an 8 mCi ^{18}F source was used. A 250–750 keV energy window was applied to each crystal to select events.

The detector temperature was controlled using an air-jet crystal cooler (Model XR401, SP Scientific, USA) and monitored by a thermocouple thermometer (Model DIGI-SENSE WD-60 010-10, Cole-Parmer Instrument Company, USA) (Du et al 2016). The probe of the thermocouple was attached to one SiPM to ensure an accurate measurement of the SiPM array's temperature.

2.3.1. Flood histograms—To determine at what settings the best flood histograms are obtained, flood histograms were measured at different overvoltages (from 1.5 V to 7.0 V, in 0.5 V intervals) and at four different temperatures (−7 °C, 0 °C, 10 °C and 20 °C) using a reference detector consisting of a 16 × 16 × 16 mm^3 LYSO crystal cube coupled to an 8 × 8 array of 6.07 × 6.07 mm^2 MicroFJ-60 035 SiPMs (ON Semiconductor, USA). The distance from the radiation source to the reference detector was 2 cm and the distance from the source to the surface of the LYSO array was 8 cm. A bias voltage of 28.5 V was applied to the reference detector, whilst a coincidence timing window of 10 ns was used to select coincidence events. The flood histograms obtained under different conditions were compared using a flood histogram quality metric calculated by the ratio of the crystal separation to the spot size as previously described in Du et al 2016. A higher flood histogram quality value reflects better separation of the crystals in the flood histogram.

2.3.2. DOI resolution—The DOI resolution was measured using a reference detector consisting of a Hamamatsu photomultiplier (PMT) model R12844-10 and a 20 × 20 × 0.5 mm^3 LYSO crystal slab. The PMT, LYSO slab and ^{22}Na source were mounted on a translation table (Du et al 2018a). The distance from the radiation source to the reference detector was 10 cm and the distance from the source to the surface of the LYSO array was 8 cm, which was used to generate a narrow radiation beam with an FWHM of ~0.4 mm on the

LYSO array (Du et al 2018a). The DOI resolution was measured at five depths (from 2 mm to 18 mm, in 4 mm intervals).

Due to the geometry needed for the experimental setup, only some of the crystals in the LYSO array were irradiated and received sufficient counts for analysis in the coincidence DOI measurement, as shown in figure 3. Measurements were taken over the 14 × 14 crystals shown in the white rectangle. The overvoltage used in the DOI measurement was the optimal overvoltage obtained for the flood histograms at each temperature (table 1). The DOI resolution was not corrected for the estimated width of the radiation beam.

2.3.3. Timing resolution—Timing resolution was also measured at the optimal overvoltage found for the flood histogram at different temperatures. A 16 × 16 × 16 mm^3 LYSO crystal (wrapped with Teflon) coupled to a Hamamatsu PMT R13449-10 was used as the reference detector. The distance from the radiation source to the reference detector was 2 cm and the distance from the source to the surface of the LYSO array was 8 cm. The PMT signal was amplified using an amplifier (AD8045) and fed into a CFD (Model 584, ORTEC, USA). The PMT signal and the DOI detector signal were used as the start and stop signal for the TAC (Model 566, ORTEC, USA) respectively, and the output of the TAC signal was also digitized by the PowerDAQ board PD2MFS (Du et al 2019).

The FWFFM obtained by a Gaussian fitting to the timing spectrum was used as the timing resolution. The estimated coincidence timing resolution of two identical DOI detector modules was calculated by subtracting in quadrature the contribution of the reference detector using the following equation:

$$CTR = \sqrt{2}\sqrt{CTR_{measured}^2 - CTR_{reference\_detector}^2/2}.$$

The average and standard deviation of the timing resolution of all 625 crystals was computed.

The timing resolution of two identical reference detectors was 398.7 ± 9.9 ps.

2.3.4. Effect of activity—The performance of PET detectors is affected by the activity of the radiation source (Du et al 2018b). For human brain studies with a ^{11}C tracer, the activity in the brain region can be on the order of ~2 mCi at the beginning of the study (Myers 2001, Chauveau et al 2008). In a preclinical study, activities are lower, for example in a mouse study, a ~100 – 200 μCi injected dose is typically used (Myers 2001, Hutchins et al 2008, Lancelot and Zimmer 2010). To investigate the performance of the detector as a function of activity, an 8 mCi FDG with a size of 10 × 10 × 8 mm^3 located 11 cm from the front of the LYSO array was used. An LYSO cylinder with a diameter of 25 mm and a length of 30 mm coupled to a Hamamatsu PMT R12844-10 was used as a reference detector. Coincidence events were acquired for ten halflives as the source decayed and flood histogram quality and energy resolution were calculated. The experiment was performed at an overvoltage of 5.0 V and a temperature of 0 °C.

3. Results

3.1. Signal shape

Figure 4 (left) shows the normalized pulse shapes of the timing signal obtained by coupling a 1 × 1 × 5 mm^3 LYSO to four different SiPMs (figure 4 (right)). The pulse shapes were the average of 200 pulses captured by an oscilloscope (Tektronix DPO7254). The sampling rate was 40 GSPS, the temperature was ~25 °C and the overvoltage was 4.5 V. To generate the pulse shapes shown in figure 4, the amplitudes of the 200 pulses obtained from one location were first individually normalized and then summed and averaged to give an average pulse.

The signal shapes and the rise times of the signal vary with location on the array, as different SiPMs were subjected to different RC values in the readout circuit. The rise times were 44.23 ± 1.10 ns, 40.32 ± 1.17 ns, 32.69 ± 1.07 ns, 30.84 ± 1.07 ns when the LYSO crystal was coupled to SiPM P1, P2, P3, and P4, respectively.

3.2. Flood histograms

The optimal flood histograms obtained at different temperatures are shown in figure 5. Figure 6 shows the flood histogram quality versus overvoltage and temperature. Improved flood histograms were obtained at lower temperatures, as this decreases the noise of the SiPM at a fixed overvoltage. For a fixed temperature, the flood histogram quality first increases and then decreases as overvoltage increases, a trend observed with other SiPM-based detectors we have evaluated (Du et al 2018b). At low overvoltages, the flood histogram quality increases with increasing voltage because the photon detection efficiency (PDE) increases and, thus, the collected photon statistics improves. Above the optimal overvoltage, the effect of the noise increases more quickly than that of the PDE, leading to a deterioration in flood histogram quality. The optimal overvoltage and the flood histogram quality value obtained at these optimal overvoltages for different temperatures are listed in table 1. The optimal overvoltage for the flood histogram was observed to be lower at higher temperatures, due to the competition of the PDE and the noise (Piemonte et al 2013).

3.3. Energy resolution

The energy resolutions were calculated using the data obtained for the flood histograms. The energy spectra of a corner, edge, and a center crystal are shown in figure 7 (left). The amplitude of the 511 keV photopeak for each crystal in the LYSO array is shown in figure 7 (right). These measurements were obtained at an overvoltage of 5.0 V and a temperature of 0 °C. The energy spectra and the photopeak positions of 511 keV photons are crystal-dependent, due to different degrees of light loss and light cross-talk among different crystals in the array.

Figure 8 shows the average energy resolution across the LYSO array as a function of overvoltage and temperature. The energy resolution was not corrected for saturation as we found the saturation was negligible due to the small microcell size (15 μm) of the SiPMs. The average energy resolution improves with the increasing overvoltage as the PDE increases, except at 20 °C. The average energy resolution obtained at 20 °C decreases when the overvoltage exceeds 5.0 V, due to the rapid increase in the noise of the SiPMs which

exceeds the effect of the increase in the PDE. While there is a tendency towards better energy resolution with lower temperatures, the effects were small.

3.4. DOI resolution

Figure 9 (left) shows the DOI profiles of an edge crystal and figure 9 (right) shows the average DOI resolution across the five depths for each of the 14 × 14 selected crystals (figure 3). The average DOI resolution of the first column of crystals and all 196 selected crystals obtained using a crystal level calibration are listed in table 2 (Yang et al 2009). The DOI resolution obtained using detector level calibration are also listed in table 2 (Yang et al 2009). Better DOI resolution was obtained at lower temperatures, however, the temperature effect on DOI resolution was quite small. The average DOI resolution obtained using the first column of crystals is better than that of all 196 selected crystals, as these outer crystals have less influence from Compton scatter, and also the width of the collimating beam was at its smallest extent at this location. This is further seen in figure 9 (right).

3.5. Timing resolution

Figure 10 shows the timing spectra for three crystals, and figure 11 (left) shows the timing offset of the timing spectra for each crystal in the LYSO array, which were obtained at an overvoltage of 5.0 V and a temperature of 0 °C. The offsets of the timing spectra are crystal-dependent, however they show a clear spatial pattern, which could be easily corrected (Wu et al 2009). The timing spectra obtained from center crystals showed a bigger timing offset compared to those obtained from the edge and corner crystals, which is in concordance with the slower rise time measured from the center crystals as shown in figure 4.

The CTR obtained at an overvoltage of 5.0 V and a temperature of 0 °C for each crystal in the LYSO array is shown in figure 11 (right). The average CTR across all crystals versus temperature is shown in figure 12. The CTR increases as the temperature increases, due to the increasing noise of the SiPMs with increasing temperature.

3.6. Effect of activity

Figure 13 shows the flood histograms obtained at different source activities, and figure 14 shows the flood histogram quality and energy resolution versus activity. It is obvious that at very high activity conditions, the flood histogram and energy resolution are both degraded, due to pulse pileup. However, all the crystals are resolved at an activity of 2 mCi which is readily sufficient for human brain imaging applications where <2 mCi is typically in the field of view of the scanner.

Figure 15 shows the estimated (red line) and the measured (blue line) single event rates on the detector approximating the source as a point source, and includes the contribution from the ^{176}Lu background from LYSO. The estimated event rates were calculated using the activity of the source and the distance of the detector to the source. The estimated event rates are higher than the measured event rates because a small lower threshold was applied to the measured event rates. The LYSO background causes the event rate to be nonlinear with activity at low source activities. At higher activities, the effect of deadtime can be seen.

The estimated event rate and the measured event rate were 240 000 and 210 000 respectively at an activity of 2 mCi, showing that the count loss due to deadtime at this activity is manageable.

4. Conclusions and discussions

A high resolution DOI detector module that could be used both for small animal PET and human brain PET scanners was evaluated experimentally. The DOI detector module consisted of two 16 × 16 SiPM arrays with a pitch size of 1.2 mm coupled to both ends of a 25 × 25 LYSO array with a pitch size of 0.75 mm and a length of 20 mm. The detector module has a packing fraction up to 95%, using very small SiPMs to minimize the gap needed between detector modules, and thus improve the sensitivity.

A simple signal multiplexing method we previously proposed was used to simplify the readout electronics. In this method, the anodes/cathodes of the SiPM array in the same row/column were connected together directly to form row/column signals. The signals of each 16 × 16 SiPM array was reduced to 16 row signals and 16 column signals using 96 passive components (capacitors and resistors), greatly simplifying the readout electronics.

The flood histograms show that all the crystals in the LYSO array were clearly resolved, except some edge crystals, due to slight mispositioning between the LYSO array and the SiPM arrays. The active area of the SiPM array is 19.0 × 19.0 mm^2, while the LYSO array has a size of 18.75 × 18.75 mm^2, making it is difficult to locate the LYSO array exactly on the center of the SiPM array. The optimal overvoltage for the flood histogram is temperature dependent due to the competition between increasing PDE (as the bias voltage is increased) and increasing noise (at the temperature or the bias voltage is increased). An overvoltage of 5.0 V at a temperature of 0 °C gave the best results without resorting to higher levels of cooling that would be more challenging to realize in a scanner.

The average energy resolution and average coincidence timing resolution both degraded with increasing temperature, due to increasing noise. The energy resolution and timing resolution obtained at an overvoltage of 5.0 V and a temperature of 0 °C were 18.4 ± 4.5% and 1.70 ± 0.12 ns respectively, adequate for small animal and human brain PET applications. Brain PETs with a timing resolution better than 250 ps timing resolutions are also under development (Akamatsu et al 2019, Takyu et al 2020), however, it is difficult to obtain a good enough timing from LSO/LYSO array with small pitch size and long length (Gundacker et al 2014, Lecoq 2017, Gundacker et al 2020). A tread-off between crystal size (spatial resolution and sensitivity) and timing resolution is always required, and we focused on spatial resolution and sensitivity in this paper.

The DOI resolution was ~2.2 mm, which is better than previously reported by ourselves and other investigators using the dual-ended readout method (Ito et al 2011, Ren et al 2014, Du et al 2018a). We believe this was due to the small microcell size (15 μm) of the SiPMs which leads to a large dynamic range, and reduces the chances of saturation. Good DOI is critical for high-resolution PET scanners with a small diameter (such as compact human brain and

small animal PET scanners) to obtain uniform resolution across the whole field of view (James et al 2010).

The proposed DOI detector module can handle an activity up to 2 mCi located 11 cm from the LYSO array, which corresponds to an activity of ~5 mCi located at 18 cm (for human brain PET), or an activity of 600 μCi located at 6 cm (for small animal PET). These results show that this detector module can be used beyond the activity levels typically encountered in these applications without excessive pileup or deadtime. Overall, the proposed PET detector module shows attractive performance parameters and could be used as the basis for future high-resolution human brain and small-animal PET scanners.

Acknowledgments

This work was funded by NIH grant R01 EB019439. The authors would like to thank Yuji Iwai and William Hendricks of Hamamatsu K K for providing the SiPM arrays, and Yu Wang of Sichuan Tianle Photonics Co., Ltd. for providing the LYSO array.

References

Akamatsu G, Yoshida E, Tashima H, Iwao Y, Takahashi M, Yamashita T and Yamaya T 2019 NEMA NU2-like performance evaluation of a helmet-type brain TOF-PET prototype J. Nucl. Med 60 192 [PubMed: 29777009]

Bertoglio Det al. 2019 Validation and noninvasive kinetic modeling of [^{11}C]UCB-J PET imaging in mice J. Cereb. Blood Flow Metab 40 1351–62 [PubMed: 31307287]

Chauveau F, Boutin H, Van Camp N, Dollé F and Tavitian B 2008 Nuclear imaging of neuroinflammation: a comprehensive review of [^{11}C]PK11195 challengers Eur. J. Nucl. Med. Mol. Imaging 35 2304–19 [PubMed: 18828015]

Cherry SR, Jones T, Karp J, Qi J, Moses W and Badawi R 2018 Total-body PET: maximizing sensitivity to create new opportunities for clinical research and patient care J. Nucl. Med 59 3–12 [PubMed: 28935835]

Du J, Bai X and Cherry SR 2018a A depth-of-interaction encoding PET detector module with dual-ended readout using large-area silicon photomultiplier arrays Phys. Med. Biol 63 245019 [PubMed: 30523925]

Du J, Bai X, Gola A, Acerbi F, Ferri A, Piemonte C, Yang Y and Cherry SR 2018b Performance of a high-resolution depth-encoding PET detector module using linearly-graded SiPM arrays Phys. Med. Biol 63 035035 [PubMed: 29324437]

Du J, Bai X, Liu C, Qi J and Cherry SR 2019 Design and evaluation of gapless curved scintillator arrays for simultaneous high-resolution and high-sensitivity brain PET Phys. Med. Biol 64 235004 [PubMed: 31618708]

Du J, Yang Y, Bai X, Judenhofer M, Berg E, Di K, Buckley S, Carl J and Cherry SR 2016 Characterization of large-area SiPM array for PET applications IEEE Trans. Nucl. Sci 63 8–16 [PubMed: 27182077]

Gaudin E, Toussaint M, Thibaudeau C, Paillé M, Fontaine R and Lecomte R 2019 Performance simulation of an ultrahigh resolution brain PET scanner using 1.2-mm pixel detectors IEEE Trans. Rad. Plas. Med. Sci 3 334–42

Gonzalez AJ. et al. 2018; Feasibility study of a small animal PET insert based on a single LYSO monolithic tube. Front. Med. 5 :328.

Gundacker S, Knapitsch A, Auffray E, Jarron P, Meyer T and Lecoq P 2014 Time resolution deterioration with increasing crystal length in a TOF-PET system Nucl. Instrum. Methods. Phys. Res. A 737 92–100

Gundacker S, Turtos R, Kratochwil N, Pots R, Paganoni M, Lecoq P and Auffray E 2020 Experimental time resolution limits of modern SiPMs and TOF-PET detectors exploring different scintillators and Cherenkov emission Phys. Med. Biol 65 02500162

Hutchins G, Miller M, Soon V and Receveur T 2008 Small animal PET imaging Ilar J. 49 54–65 [PubMed: 18172333]

Ito M, Hong S and Lee J 2011 Positron emission tomography (PET) detectors with depth-of-interaction (DOI) capability Biomed. Eng. Lett 1 70–81

James S, Yang Y, Bowen S L, Qi J and Cherry SR 2010 Simulation study of spatial resolution and sensitivity for the tapered depth of interaction PET detectors for small animal imaging Phys. Med. Biol 55 N63 [PubMed: 20023331]

Kochebina O, Jan S, Stute S, Sharyy V, Verrecchia P, Mancardi X and Yvon D 2019 Performance estimation for the high resolution CaLIPSO brain PET scanner: a simulation study IEEE Trans. Rad. Plas. Med. Sci 3 363–70

Lancelot S and Zimmer L 2010 Small-animal positron emission tomography as a tool for neuropharmacology Trends Pharmacol. Sci 31 411–7 [PubMed: 20599282]

Lecoq P 2017 Pushing the limits in time-of-flight PET imaging IEEE Trans. Rad. Plas. Med. Sci 1 473–85

Lehnert W, Gregoire MC, Reilhac A and Meikle SR 2012 Characterisation of partial volume effect and region-based correction in small animal positron emission tomography (PET) of the rat brain Neuroimage 60 2144–57 [PubMed: 22387126]

Lubberink M and Heurling K 2019 Kinetic modeling of radiotracers Radiopharmaceutical Chemistry eds Lewis J et al. (Berlin: Springer) (10.1007/978-3-319-98947-1_28)

Myers R 2001 The biological application of small animal PET imaging Nucl. Med. Bio 28 585–93 [PubMed: 11516702]

Nørgaard M, Ganz M, Svarer C, Frokjaer V, Greve D, Strother S and Knudsen G 2019 Optimization of preprocessing strategies in positron emission tomography (PET) neuroimaging: A [^{11}C]DASB PET study NeuroImage 199 466–79 [PubMed: 31158479]

Park H and Lee J 2019 Highly multiplexed SiPM signal readout for brain-dedicated TOF-DOI PET detectors Phy. Med 68 117–23

Piemonte C, Ferri A, Gola A, Pro T, Serra N, Tarolli A and Zorzi N 2013 Characterization of the first FBK high-density cell siliconphotomultiplier technology IEEE Trans. Electron Devices 60 2567–73

Pizzichemi M, Polesel A, Stringhini G, Gundacker S, Lecoq P, Tavernier S, Paganoni M and Auffray E 2019 On light sharing TOF-PET modules with depth of interaction and 157 ps FWHM coincidence time resolution Phys. Med. Biol 64 155008 [PubMed: 31239430]

Popov V, Majewski S and Weisenberger A 2003 Readout electronics for multianode photomultiplier tubes with pad matrix anode layout IEEE Nucl. Sci. Symp. Conf. Rec. (Portland, OR, USA, 19–25 October 2003) (10.1109/NSSMIC.2003.1352307)

Ren S, Yang Y and Cherry SR 2014 Effects of reflector and crystal surface on the performance of a depth-encoding PET detector with dual ended readout Med. Phys 41 072503 [PubMed: 24989406]

Shao Y, Sun X, Lan K, Bircher C, Lou K and Deng Z 2014 Development of a prototype PET scanner with depth-of-interaction measurement using solid-state photomultiplier arrays and parallel readout electronics Phys. Med. Biol 59 1223–38 [PubMed: 24556629]

Takyu S, Ahmed A, Yoshida E, Tashima H, Kumagai M, Yamashita T and Yamaya T 2020 Design study of a brain-dedicated time-of-flight PET system with a hemispherical detector arrangement Phys. Med. Biol 65 035012 [PubMed: 31855854]

Wu Y, Ng T, Yang Y, Shah K, Farrell R and Cherry SR 2009 A study of the timing properties of position-sensitive avalanche photodiodes Phys. Med. Biol 54 5155–72 [PubMed: 19671971]

Yamamoto S, Watabe H, Watabe T, Ikeda H, Kanai Y, Ogata Y, Kato K and Hatazawa J 2016 Development of ultrahigh resolution Si-PM based PET system using 0.32 mm pixel scintillators Nucl. Instrum. Methods. Phys. Res. A 836 7–12

Yamamoto S, Yeom J, Kamada K, Endo T and Levin C 2013 Development of an ultrahigh resolution block detector based on 0.4 mm pixel Ce: gAGGscintillators and a silicon photomultiplier array IEEE Trans. Nucl. Sci 60 4582–7

Yang Q, Kuang Z, Sang Z, Yang Y and Du J 2019 Performance comparison of two signal multiplexing readouts for SiPM-based PET detector Phys. Med. Biol 64 23NT02

Yang Y et al. 2016 A prototype high-resolution small-animal PET scanner dedicated to mouse brain imaging J. Nucl. Med 57 1130–5 [PubMed: 27013696]

Yang Y, Qi J, Wu Y, James S St, Farrell R, Dokhale PA, Shah KS and Cherry SR 2009 Depth of interaction calibration for PET detectors with dual-ended readout by PSAPDs Phys. Med. Biol 54 433–45 [PubMed: 19098356]

Zuo Y, Sarkar S, Corwin M, Olson K, Badawi R and Wang G 2019 Structural and practical identifiability of dual-input kinetic modeling in dynamic PET of liver inflammation Phys. Med. Biol 64 175023 [PubMed: 31051490]

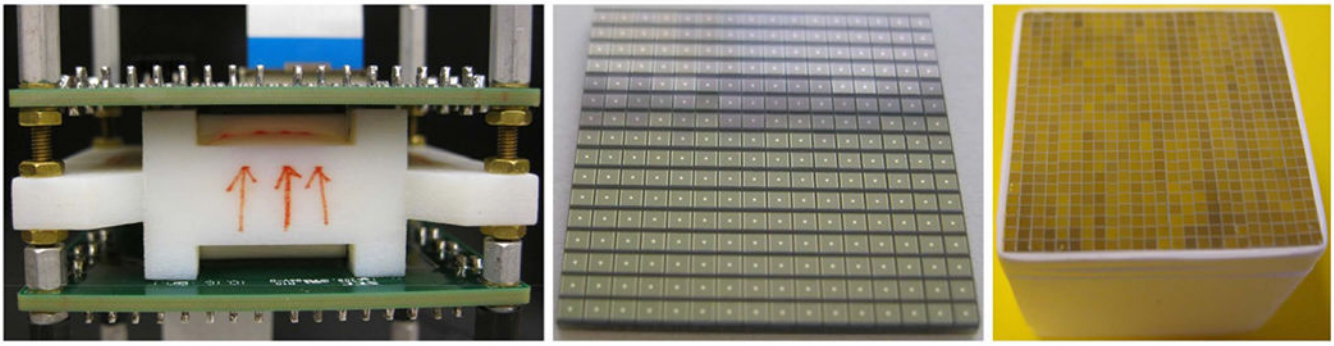

Figure 1.
Photographs of (left) the DOI detector module, (middle) the SiPM array, and (right) the LYSO array.

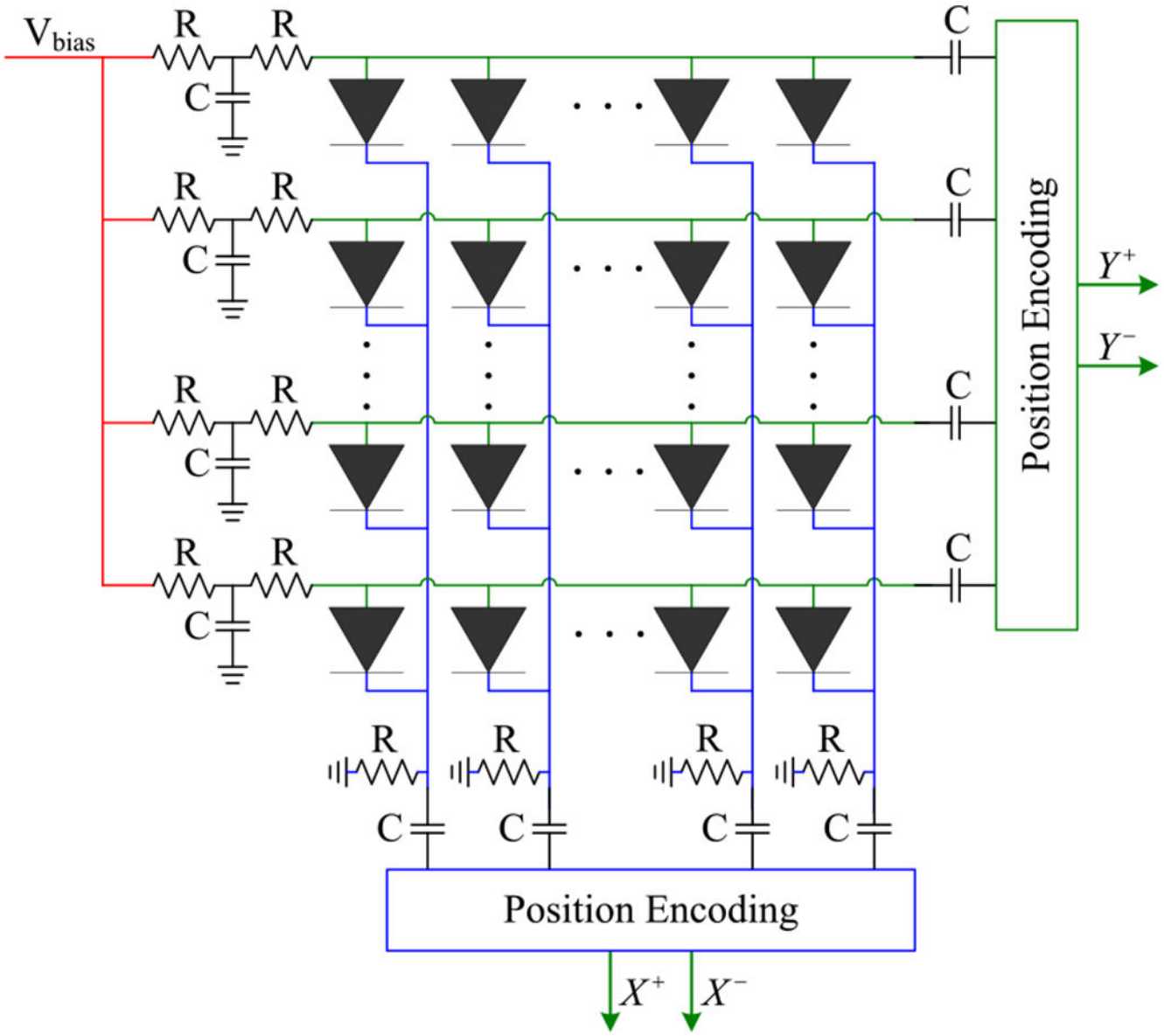

Figure 2.
Schematic showing signal multiplexing method.

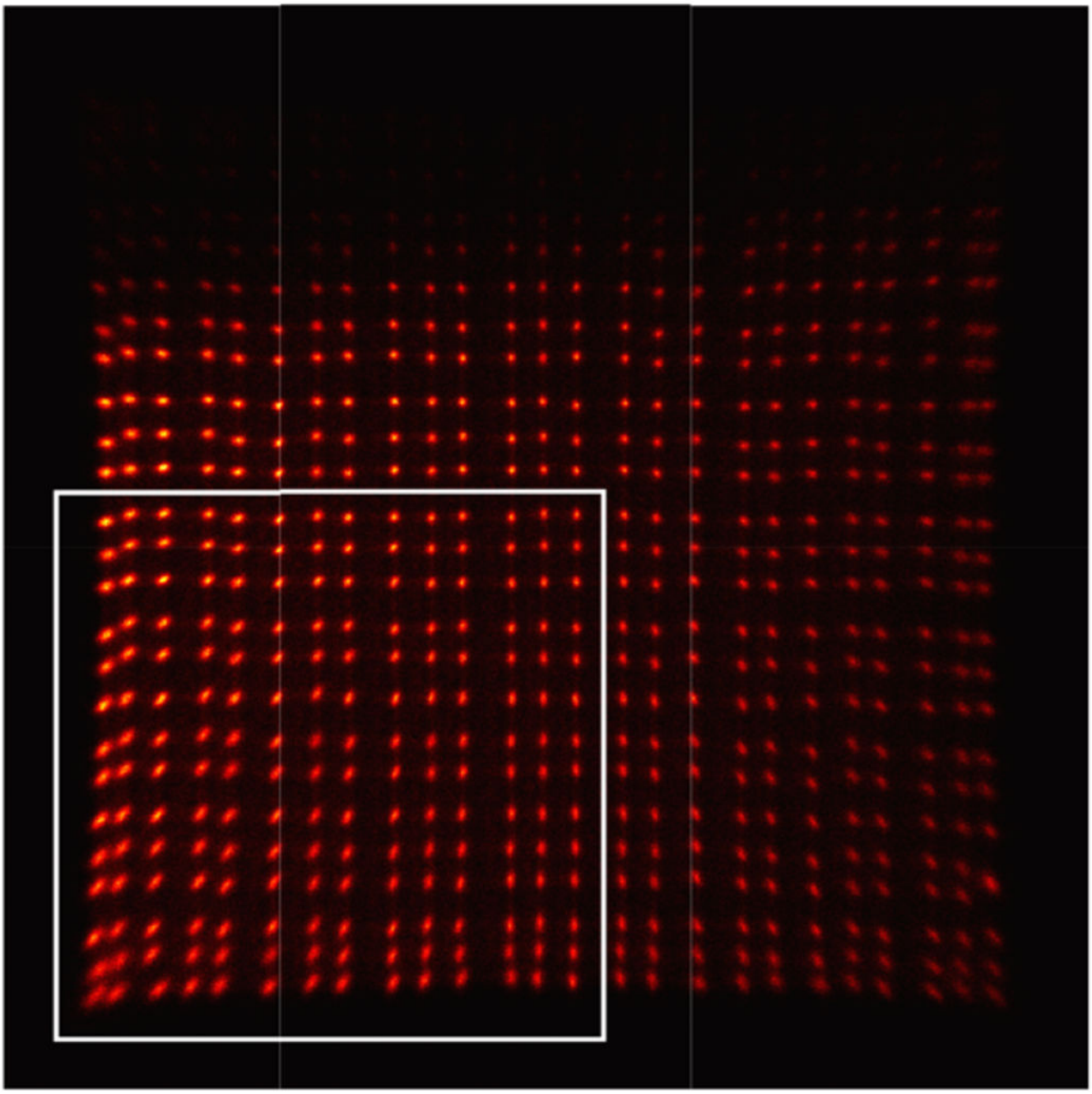

Figure 3.
Flood histogram obtained during DOI resolution measurements. The 196 crystals in the white rectangle were used in the analysis.

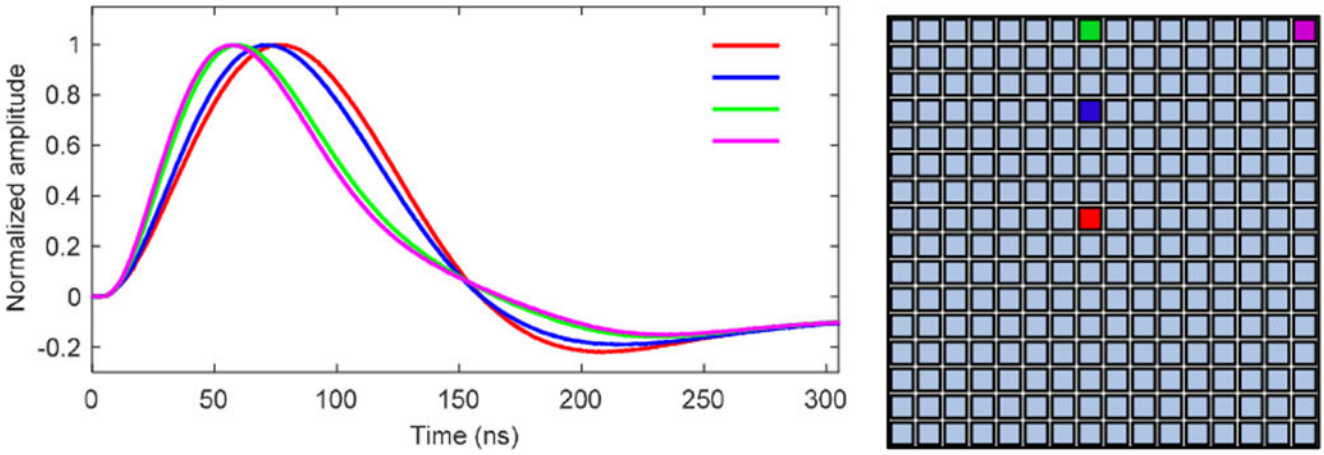

Figure 4.

(left) average pulse shapes obtained by coupling a 1 × 1 × 5 mm^3 LYSO to (right) four different SiPMs. The location of each SiPM P1-P4 is color coded as indicated.

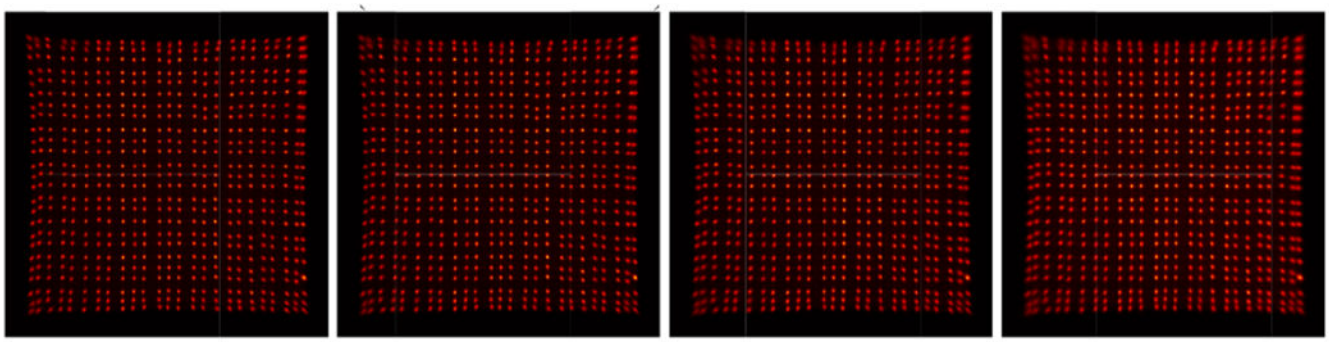

Figure 5.

Optimal flood histograms obtained at different temperatures. From left to right, overvoltages were 5.4 V, 5.0 V, 4.9 V and 4.3 V, and the temperatures were −7 °C, 0 °C, 10 °C and 20 °C.

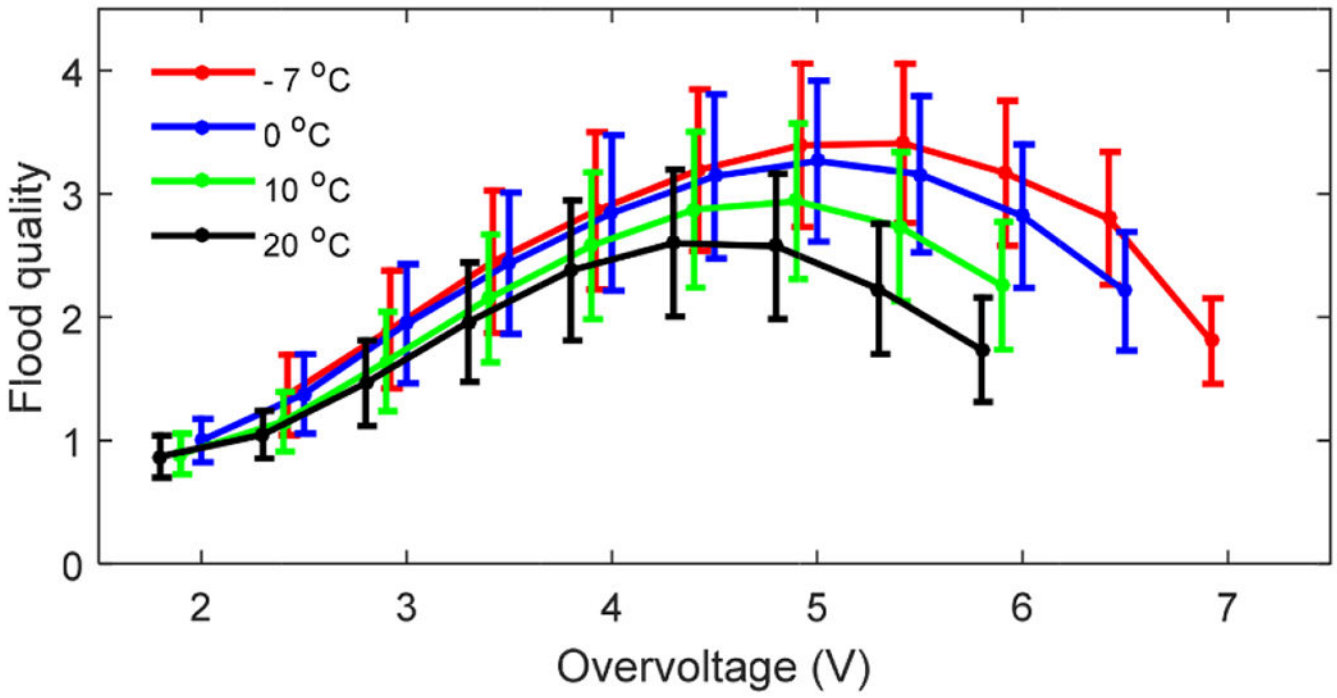

Figure 6.
Flood histogram quality value versus overvoltage and temperature. The error bars are the standard deviation value of flood quality across all crystals.

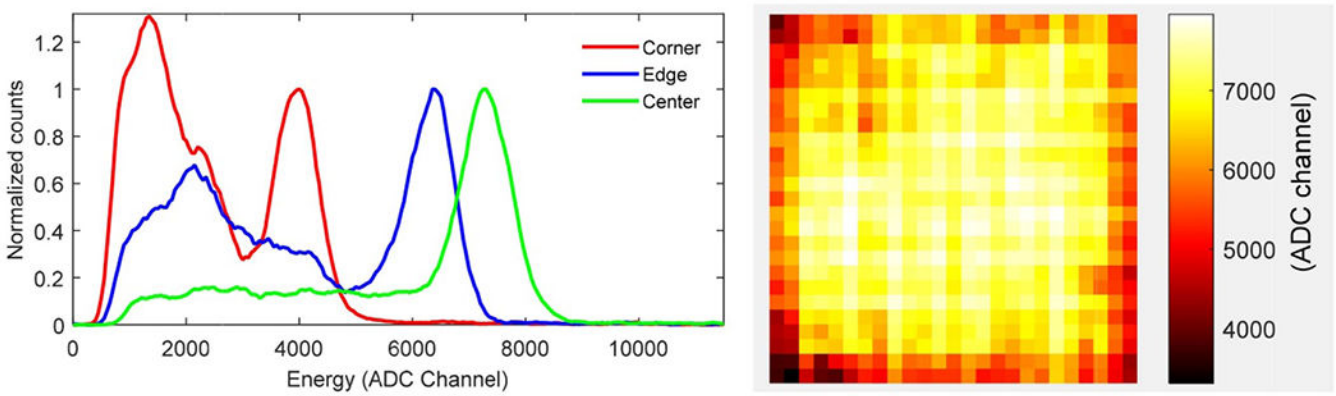

Figure 7.

(left) energy spectra of a corner, edge, and center crystal, and (right) 511 keV photopeak position for each crystal in the LYSO array Measurements were obtained at an overvoltage of 5.0 V and a temperature of 0 °C.

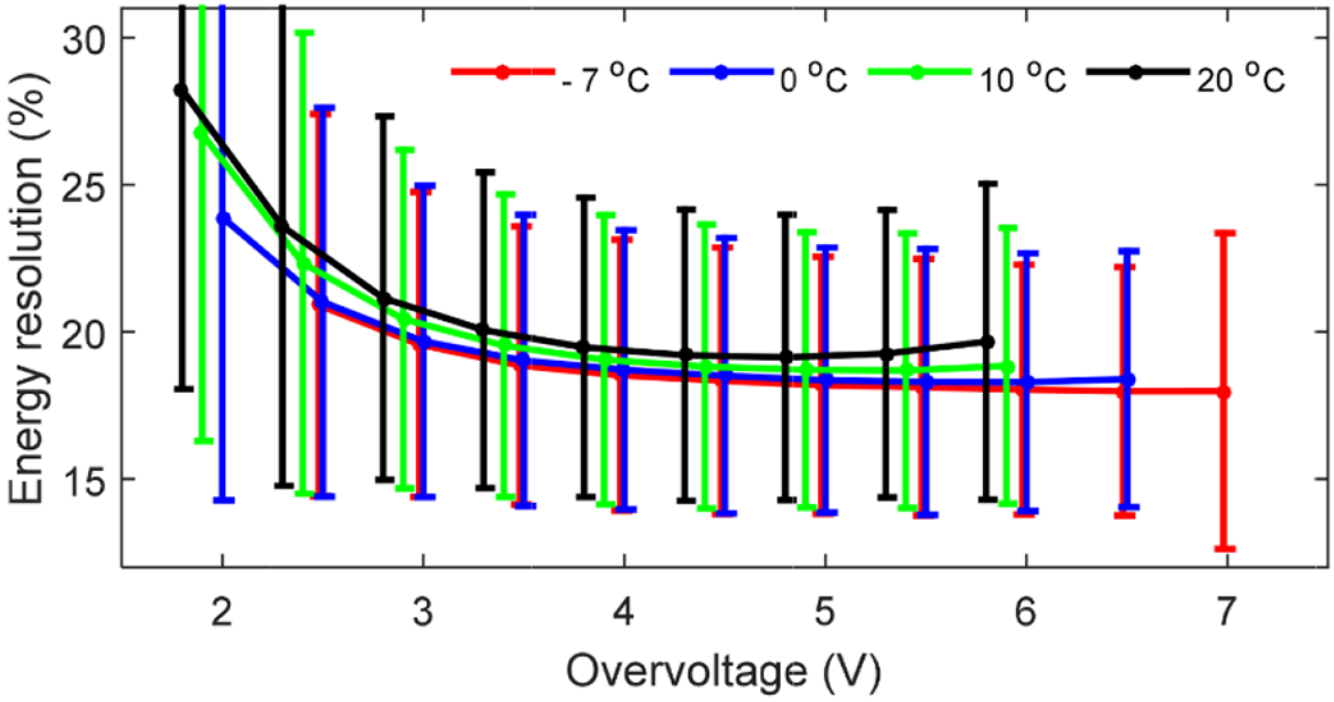

Figure 8.

Average energy resolution versus overvoltage and temperature. The large error bars reflect the wide variations in energy resolution across crystals depending on the variations in light coupling from each crystal into the SiPM array (see figure 7, right). The error bars are the standard deviation value of energy resolution across all crystals.

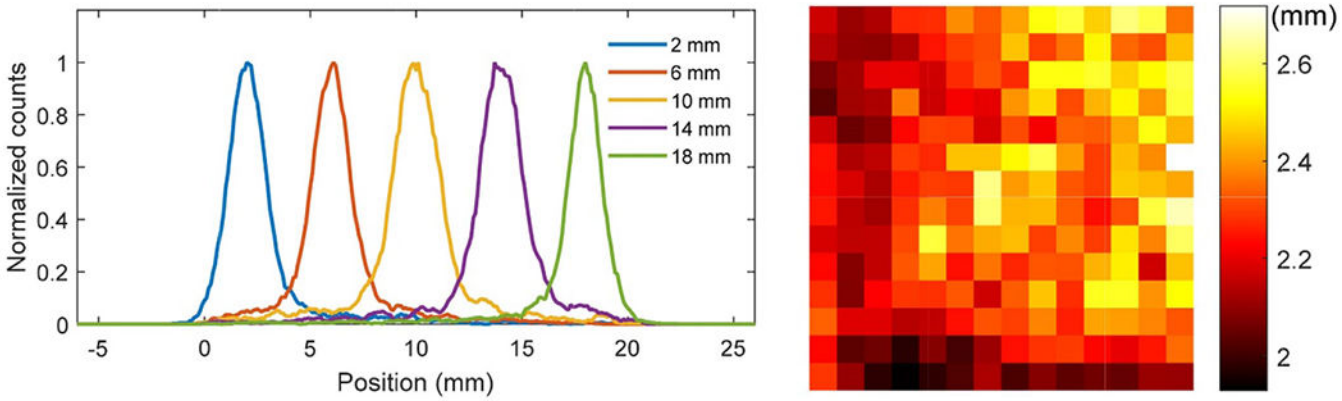

Figure 9.

(left) DOI profiles of an edge crystal and (right) average DOI resolution across the five depths for each of the selected 14 × 14 crystals. The histogram on the right is in the same orientation as indicated on figure 3 (i.e. center of detector block is at upper right corner). Measurements were obtained at an overvoltage of 5.0 V and a temperature of 0 °C.

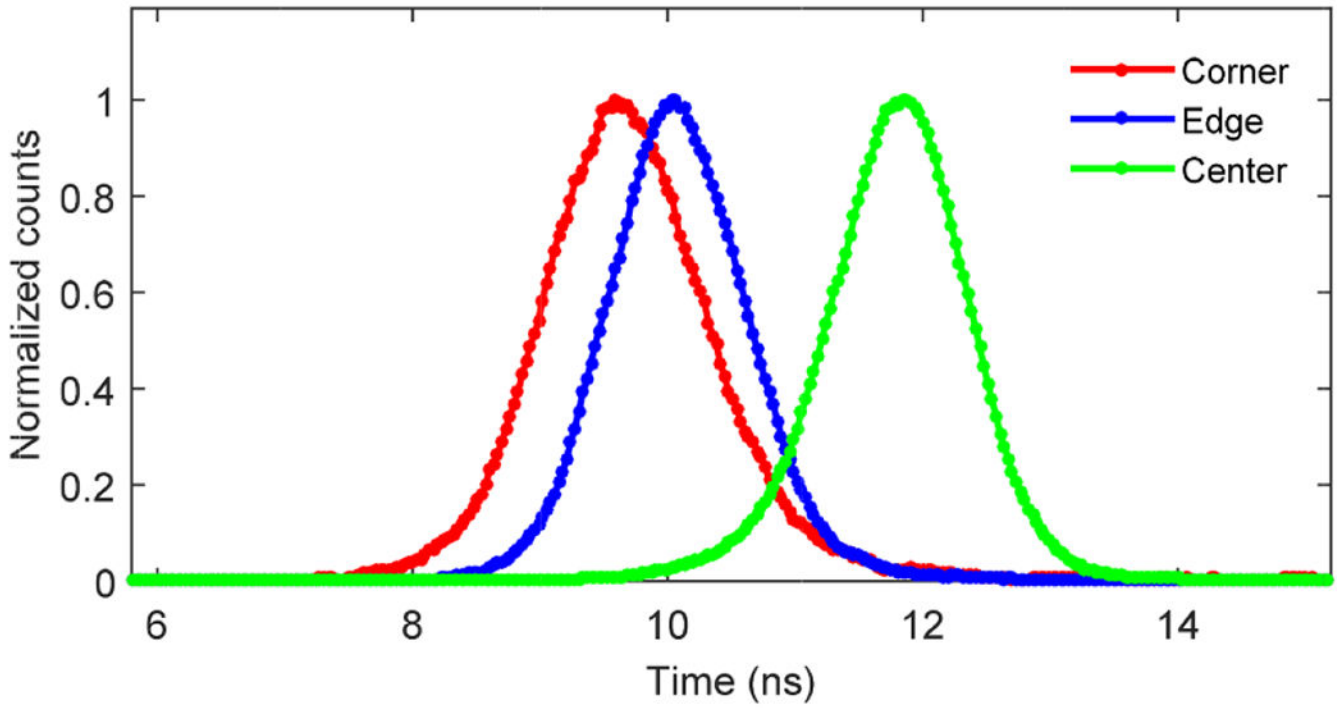

Figure 10.
Timing spectra of a corner, edge, and a center crystal, obtained at an overvoltage of 5.0 V and a temperature of 0 °C.

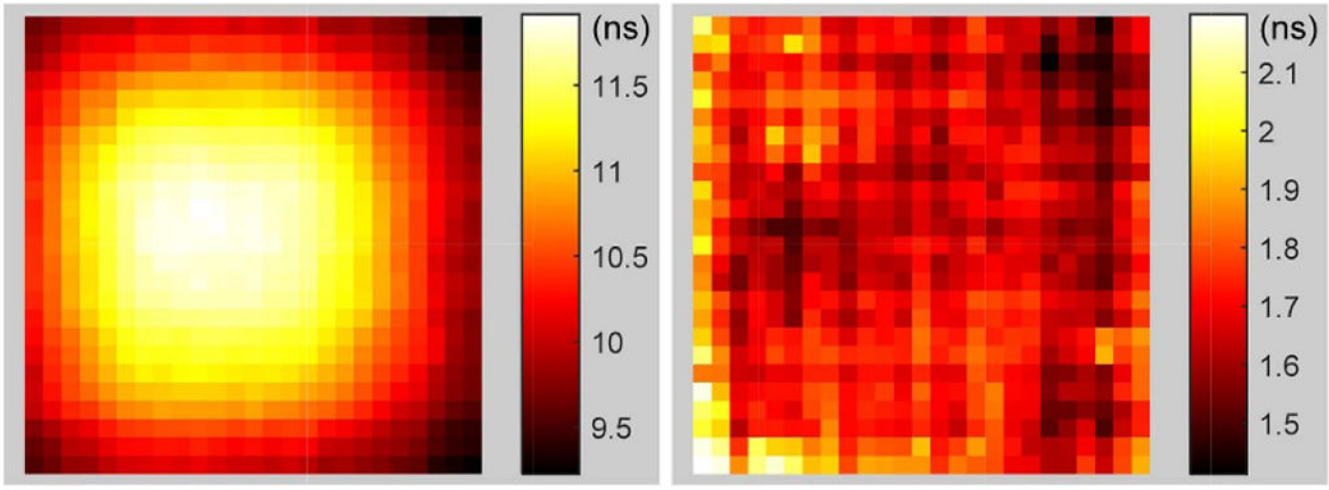

Figure 11.

(left) the offset of the timing spectra and (right) the coincidence timing resolution for each crystal. Measurements were obtained at an overvoltage of 5.0 V and a temperature of 0 °C.

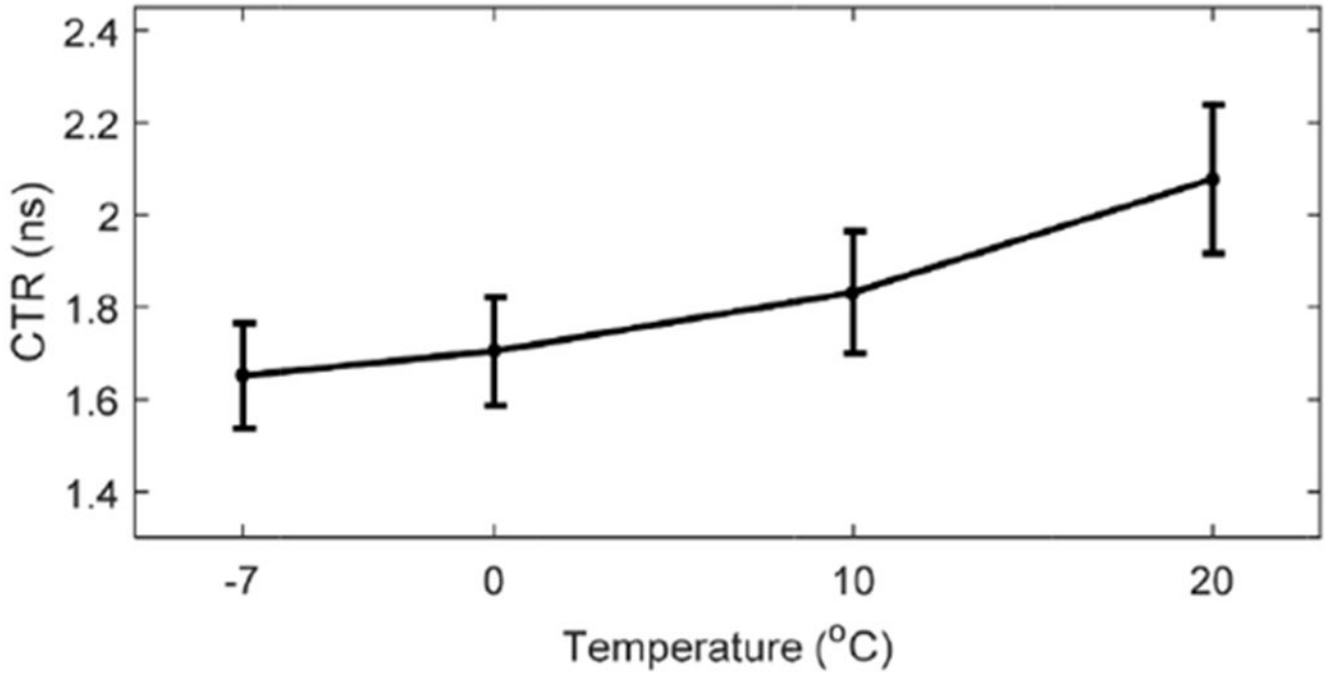

Figure 12.
Average timing resolution versus temperature. The error bars are the standard deviation value of timing resolution across all crystals.

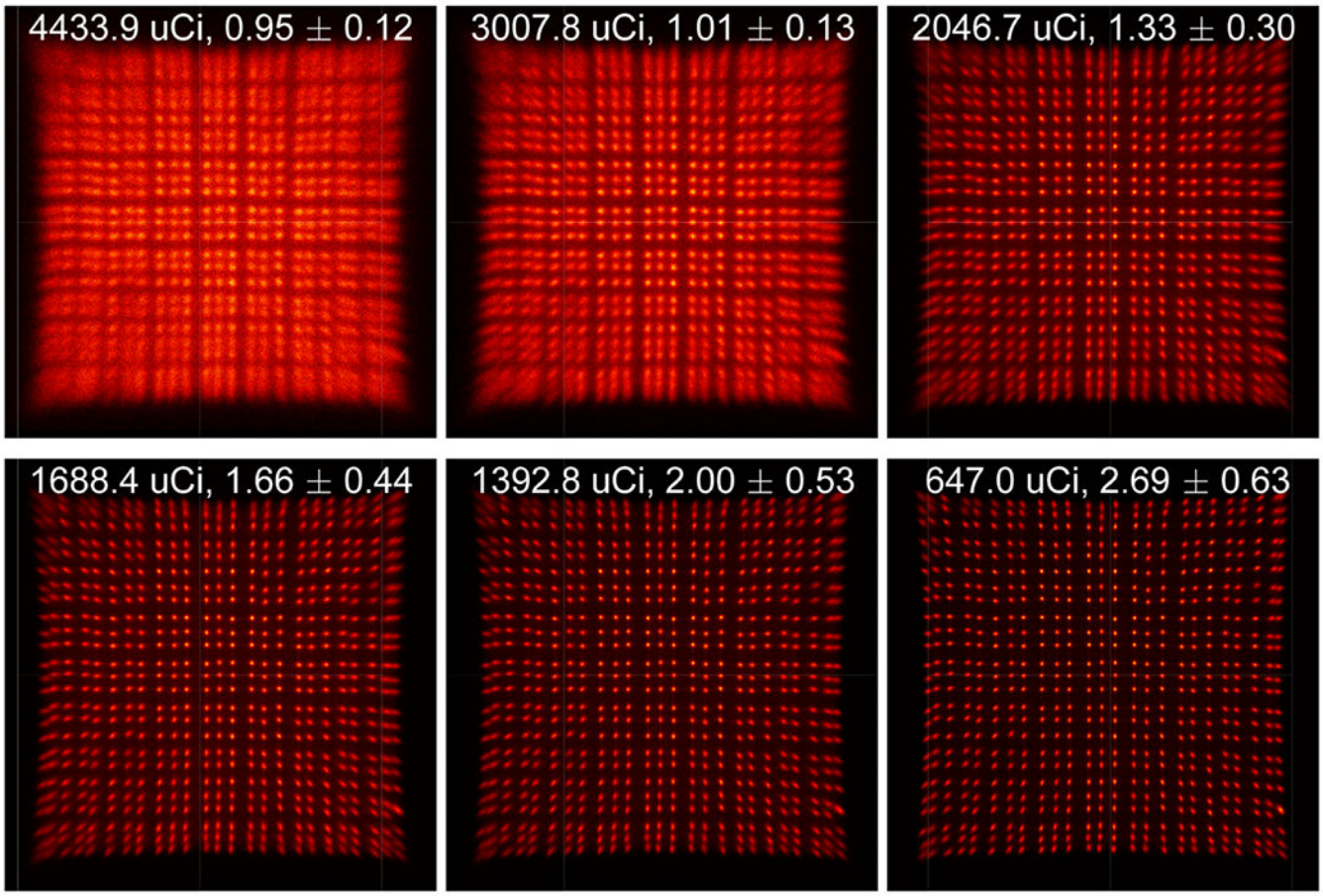

Figure 13.
Flood histogram obtained at different source activities. The overvoltage was 5.0 V and the temperature was 0 °C.

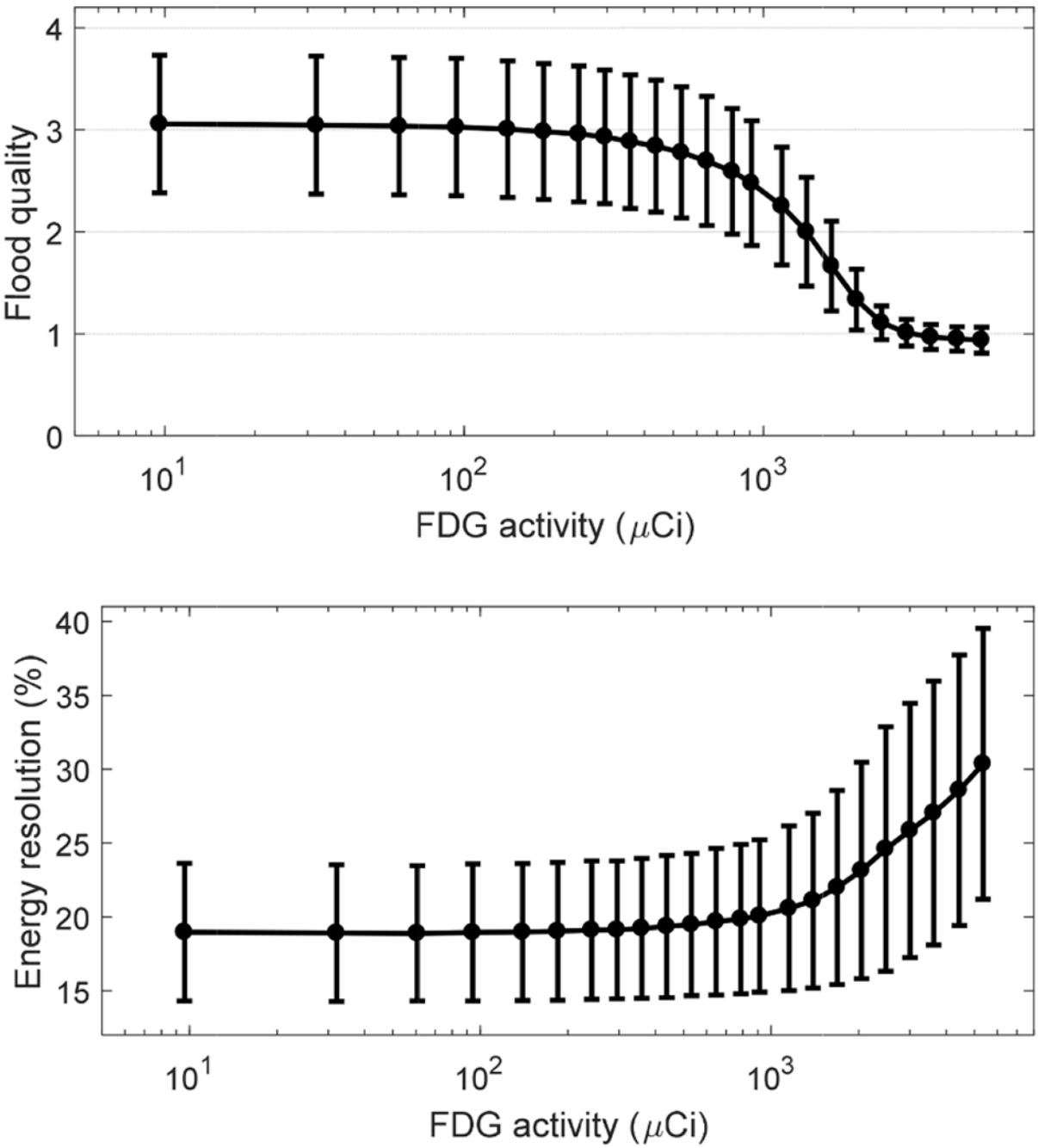

Figure 14.

(top) Flood histogram quality and (bottom) average energy resolution versus activity. The overvoltage was 5.0 V and the temperature was 0 °C. The error bars are the standard deviation value of flood quality (top) and energy resolution (bottom) across all crystals.

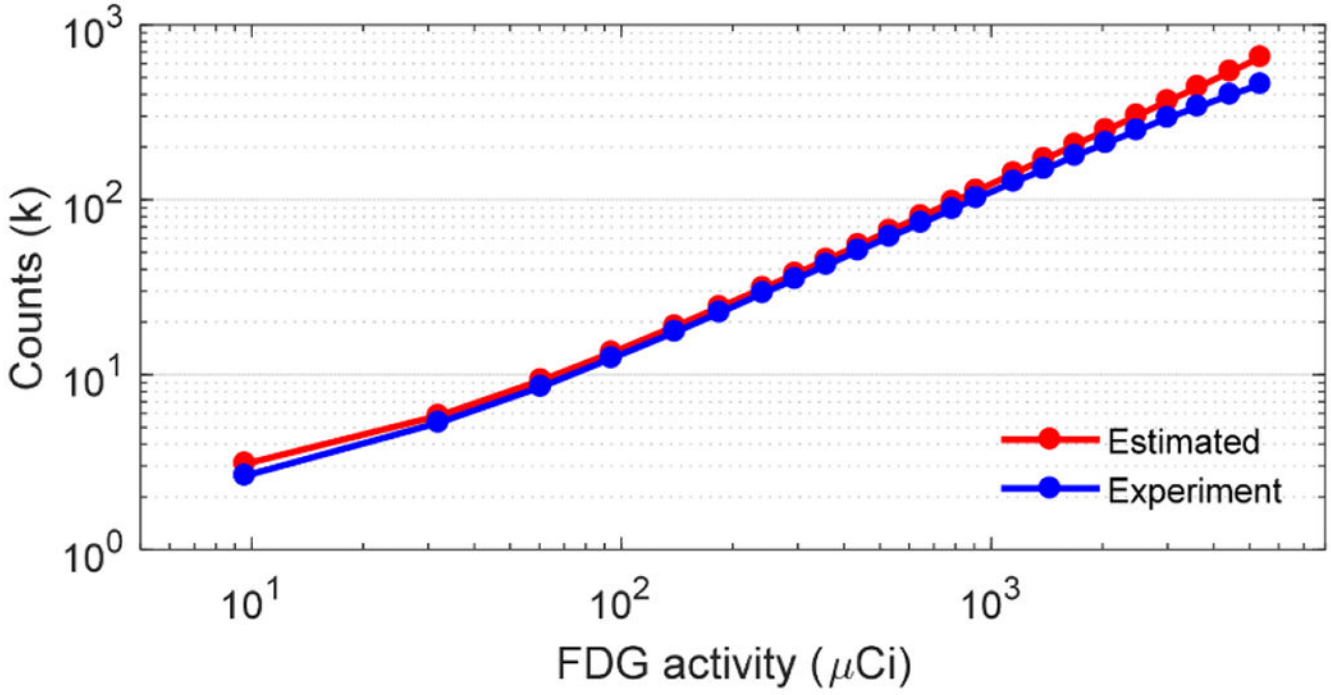

Figure 15.
The estimated (red line) and measured (blue line) single event rates at different activities.

Table 1.

Optimal overvoltage and the flood histogram quality value obtained at the optimal overvoltage as a function of temperature.

Temperature (°C)	Overvoltage (V)	Flood histogram quality
−7	5.4	3.4 ± 0.6
0	5.0	3.3 ± 0.7
10	4.9	2.9 ± 0.6
20	4.3	2.6 ± 0.6

Table 2.

DOI resolution versus temperature.

Temperature /°C	Crystal level calibration/mm		Detector level calibration /mm
	First column crystals	All 196 crystals	
−7	2.20 ± 0.20	2.28 ± 0.27	2.64 ± 0.16
0	2.22 ± 0.19	2.30 ± 0.27	2.65 ± 0.16
10	2.22 ± 0.22	2.30 ± 0.27	2.68 ± 0.20
20	2.27 ± 0.20	2.41 ± 0.32	2.77 ± 0.38